ORIGINAL ARTICLE

Cytometry PART A
Journal of the International Society for Advancement of Cytometry

Quantification of Cardiomyocyte Contraction Based on Image Correlation Analysis

A. Kamgoué,[1] J. Ohayon,[1]* Y. Usson,[2] L. Riou,[3] P. Tracqui[1]*

[1]Equipe DynaCell, Laboratoire TIMC-IMAG, UMR CNRS 5525, Institut de l'Ingénierie et de l'Information de Santé, (In3S), Faculté de Médecine de Grenoble, 38706 La Tronche Cedex, France

[2]Equipe RFMQ, Laboratoire TIMC-IMAG, UMR CNRS 5525, Institut de l'Ingénierie et de l'Information de Santé, (In3S), Faculté de Médecine de Grenoble, 38706 La Tronche Cedex, France

[3]INSERM U877, Radiopharmaceutique biocliniques, Faculté de Médecine de Grenoble, 38706 La Tronche Cedex, France

Received 26 June 2008; Revision Received 28 October 2008; Accepted 25 November 2008

Contract grant sponsors: Fondation d'Entreprise Groupe Banque Populaire, Bâtir votre Projet—Jeunes Handicapés Physiques.

*Correspondence to: J. Ohayon, Equipe DynaCell, Laboratoire TIMC-IMAG, In3S, Faculté de Médecine de Grenoble, 38706 La Tronche Cedex, France.
Email: jacques.ohayon@imag.fr or P. Tracqui, Equipe DynaCell, Laboratoire TIMC-IMAG, In3S, Faculté de Médecine de Grenoble, 38706 La Tronche Cedex, France

Email: philippe.tracqui@imag.fr

Published online 23 December 2008 in Wiley InterScience (www.interscience.wiley.com)

DOI: 10.1002/cyto.a.20700

© 2008 International Society for Advancement of Cytometry

Abstract

Quantification of cardiomyocyte contraction is usually obtained by measuring globally cell shortening from the displacement of cell extremities. We developed a correlation-based optical flow method, which correlates the whole-cell temporal pattern with a precise quantification of the intracellular strain wave at the sarcomeres level. A two-dimensional image correlation analysis of cardiomyocytes phase-contrast images was developed to extract local cell deformations from videomicroscopy time-lapse sequences. Test images, synthesized from known intensity displacement fields, were first used to validate the method. Intracellular strain fields were then computed from videomicroscopy time-lapse sequences of single adult and neonatal cardiomyocytes. The propagation of the sarcomeres contraction–relaxation wave during cell contraction has been successfully quantified. The time-varying patterns of intracellular displacement were obtained accurately, even when cardiomyocyte bending occurred in pace with contraction. Interestingly, the characterization of the successive 2D displacement fields show a direct quantification of the variation with time of intracellular strains anywhere in the cell. The proposed method enables a quantitative analysis of cardiomyocyte contraction without requiring wave tracking with the use of fluorescent calcium probes. Thus, our algorithmic approach provides a fast and efficient tool for analyzing the correlation between global cell dynamical behavior and mechanosensitive intracellular processes.

© 2008 International Society for Advancement of Cytometry

Key terms

optical flow; contraction wave; image sequence analysis; intracellular strain

INTRACELLULAR Ca^{2+} waves play an integral part in the process of excitation-contraction coupling within mammalian cardiomyocytes. Ca^{2+} waves might spontaneously arise from a triggering pulse of Ca^{2+} released from the sarcoplasmic reticulum, which under certain circumstances propagates throughout the cell (1–3). The qualitative and quantitative characterization of Ca^{2+} waves, including amplitude, frequency, and propagation velocity, is thus a central issue for understanding both normal and pathological contractile cell behavior, such as the correlation of spontaneous Ca^{2+} waves with arrhythmic electrical activity (4–6). Despite obvious limitations, such analyses are usually conducted on isolated single cardiac cells. Indeed, within the myocardium, the cardiomyocytes are arranged in a complex network. Thus, correlating accurately forces and length changes with intracellular Ca^{2+} waves is rather difficult. Monitoring Ca^{2+} waves has then been made possible by using fast confocal microscopy techniques, which image the intensity variation of calcium fluorescent probes such as Fluo-3 (7,8). In addition, such probes have been proven to be highly valuable for analyzing the dynamic of intracellular Ca^{2+} components, like ryanodine receptors (9,10).

On the other hand, the direct quantification of sarcomere mechanical status becomes highly valuable to get insights into the regulation of cardiac muscle contraction mediated by the mechanosensitivity of biochemical processes or molecular interactions, which depend on the sarcomere length or on actin-myosin filaments spacing. Sarcomeres length measurements are usually based on laser diffraction techniques

ISAC
International Society for Advancement of Cytometry

(11), but this approach is not well suited for the analysis of the spatio-temporal variation of the sarcomeres length at the cell level, especially when the dynamic of the cardiomyocyte contraction wave has to be characterized.

To overcome these limitations, we developed an optical flow approach aiming at characterizing the spatio-temporal variation of intracellular strain fields associated with sarcomeres contraction–relaxation over the course of cardiomyocyte contraction. Even though optical flow methods are rather widely applied in several engineering or bioengineering fields, only a few attempts have yet been made to apply them to single cell dynamics analysis (12–14), mostly because animal cells are highly deformable objects. Among the rather large spectrum of optical flow methods implementations (15,16), Image Correlation Method (ICM) (17–19) seemed to us a quite relevant approach for characterizing intracellular strain fields during cardiomyocyte contraction. Indeed, the highly structured and anisotropic organization of the cell sarcomeres defines a very precise and repetitive spatial pattern, which may be used in a rather discriminating way by ICM when looking for a similarity between two successive patches of the region of interest (ROI) within cell images. Thus, we were expecting that such *a priori* optimality can be quantitatively assessed by developing an image-processing algorithm that takes benefit of the specific grey level patterns generated by phase contrast observation of contracting cardiac cells.

In this article, we propose and validate a complete procedure which provides an accurate estimation of the 2D displacement fields at any cardiomyocyte location from the analysis of time-lapse sequences of single cell contraction recorded using phase contrast and differential interface contrast (DIC) videomicroscopy. An essential step in this procedure is to find the displacement field, which optimizes the prediction of the light intensity pattern which will be observed when considering two successive images of the sequence. The first part of the article focuses on the method implementation. Then, our method reliability and accuracy is assessed by analyzing different sets of synthesized pair of images, constructed from known intensity displacement fields. The second part of the article is devoted to the analysis of experimental time-lapse sequences showing different spatio-temporal patterns of spontaneously contracting adult rat cardiomyocytes. For each considered experiment, the spatial distribution of intracellular strain fields has been characterized at several times during the cardiomyocyte contraction. In the discussion section, the robustness of our approach is discussed by considering less textured contracting objects. For this purpose, image sequences of spontaneously contracting neonatal cardiomyocytes have been analyzed, since at this stage of development, the cytoskeleton of these cells lacks the regular sarcomere organization present in adult cells.

Materials and Methods

Cell Culture

Adult rat cardiomyocytes were kindly provided by the LBFA laboratory (Joseph Fourier University, Grenoble). Briefly, cells were isolated from rat heart ventricles by enzymatic dissociation as described in Ref. 20.

Time-Lapse Video Microscopy

The spontaneous and periodic contractions of the isolated adult rat cardiomyocytes were recorded by DIC and phase contrast time-lapse videomicroscopy using an imaging workstation composed of an inverted microscope (Zeiss Achrostigmat Axiovert 135) equipped with a 10× objective (Zeiss Acroplan), automated shutters (Uniblitz) and a CCD camera (CoolSNAP HQ, Roper Scientific). Image acquisition was controlled via a computer using a dedicated software (Metaview, Roper Scientific). Microscope calibration was performed using a micrometric slide (PRESS-PRO21). The size of the images we analyzed was 442 × 161 pixels. Images were taken every 110 ms at room temperature.

Image Correlation Analysis and Displacement Field Computation

An ICM was used to compute the displacement field $\boldsymbol{w}(u,v)$ between a pair of successive images taken at time t and $t+\Delta t$, and labeled for convenience as *Image 1* and *Image 2*, respectively. Let us consider a small window area *Wind*1 in *Image* 1 (Fig. 1). Then, the aim of the algorithm is to find the matching window *Wind*2 in *Image* 2, i.e., the position to which *Wind*1 has moved during the time interval Δt. For this purpose, *Wind*1 is compared with windows belonging to the same neighborhood *Neigh*2 in *Image* 2 (Fig. 1). *Neigh*2 is also called the region of interest (ROI). For each window *Wind*2, a similarity measure is computed. The window exhibiting the highest similarity, i.e. the best correlation with *Wind*1, is then retained as the matching window *Wind*2*.

More formally, let us denote $\boldsymbol{I}_{W1}$ the illumination intensity matrix of *Wind*1, and $\boldsymbol{I}_{W2}$ the illumination intensity matrix of any current window *Wind*2 of the ROI, respectively, with

$$\boldsymbol{I}_{W1} = \left(I_t^{ij}\right) = \boldsymbol{I}_t(i,j) \quad \boldsymbol{I}_{W2} = \left(I_{t+\Delta t}^{ij}\right) = \boldsymbol{I}_{t+\Delta t}(i+u, j+v) \tag{1}$$

where any integer $I_t(i,j)$ defines the reference grey level value at time t of the pixel located at (i,j) in *Image* 1, while $I_{t+\Delta t}(i+u, j+v)$ defines the corresponding current grey level value of the pixel located at $(i+u, j+v)$ in *Image* 2, corresponding to time $t+\Delta t$.

For any window *Wind*1, we are looking for an optimum window *Wind*2* such that

$$\boldsymbol{C}(\boldsymbol{I}_{W1}, \boldsymbol{I}_{W2^*}) = \max_{(u^*,v^*)/\mathrm{ROI}} \{\boldsymbol{C}(\boldsymbol{I}_{W1}\boldsymbol{I}_{W2})\} \tag{2}$$

where

$$\boldsymbol{I}_{W2^*} = \left(\boldsymbol{I}_{t+\Delta t}^{ij}\right) = \boldsymbol{I}_{t+\Delta t}(i+u^*, j+v^*) \tag{3}$$

and $(u^\star,v^\star)$ are the two unknown components of the optimum displacement vector $\boldsymbol{w}^\star(u^\star,v^\star)$ with respect to the chosen similarity or discrete cross-correlation function $\boldsymbol{C}(.,.)$.

Among all different similarity functions proposed, we chose a variance-normalized cross-correlation function $C_V(.,.)$, since

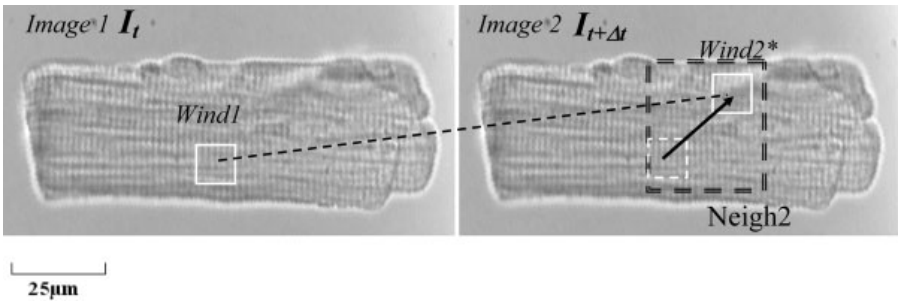

Figure 1. Background for the Image Correlation Method (ICM) developed for analyzing two successive cardiomyocte images of a videomicroscopy sequence. This optical flow method is based on the computation of a cross-correlation function between a given window *Wind1* in *Image 1* taken at time *t* (left), and all the possible matching windows *Wind2* of the same size included in a neighbourhood *Neigh2 (*dashed line boundaries) defined in the next image of the sequence, called *Image 2* and corresponding to time $t+\Delta t$ (right). In this figure, the best correlation with the image area *Wind1* has been obtained with the matching window labeled *Wind2**. The resulting displacement vector is then given by the arrow linking *Wind1* and *Wind2** centers.

such weighted criterion has been shown to be more robust (21,22).

Considering two matrices $\boldsymbol{I}_{W1}$ and $\boldsymbol{I}_{W2}$ with dimension (N,M), the similarity function $\boldsymbol{C}_V(.,.)$ is computed for each successive pair of the image sequence as

$$C_V(\boldsymbol{I}_{W1},\boldsymbol{I}_{W2}) = \frac{\sum_{i=0}^{M-1}\sum_{j=0}^{N-1}\left[I_t^{ij}-\overline{I}_t\right]\left[I_{t+\Delta t}^{ij}-\overline{I}_{t+\Delta t}\right]}{\sqrt{\sum_{i=0}^{M-1}\sum_{j=0}^{N-1}\left[I_t^{ij}-\overline{I}_t\right]^2\left[I_{t+\Delta t}^{ij}-\overline{I}_{t+\Delta t}\right]^2}} \quad (4)$$

where $\overline{\boldsymbol{I}}_t$ and $\overline{\boldsymbol{I}}_{t\,+\,\Delta t}$ represent the respective means of $\boldsymbol{I}_t$ and $\boldsymbol{I}_{t+\Delta t}$ defined as

$$\overline{I}_{W1} = \frac{\sum_{ij} I_t^{ij}}{M \times N} \quad \overline{I}_{W2} = \frac{\sum_{ij} I_{t+\Delta t}^{ij}}{M \times N} \quad (5)$$

The algorithmic strategy used for computing $\boldsymbol{w}(u,v)$ follows different guidelines. A major point is to limit the size of the ROI in order to optimize the speed, robustness, and accuracy of our algorithm. Indeed, dealing with small displacements requires considering neighborhood of small size and imposes large computational times, but choosing too large neighborhoods would likely lead to non-meaningful displacement solutions, as illustrated below.

Optimization of the ROI

Detection of the matching window *Wind2** must take care of both the displacement amplitude and of the background noise in the illumination maps, this latter originating from different sources. These include fluctuations of illumination intensity with object displacement (departure from illumination conservation assumption), as well as fluctuations of the focusing plane in the case of a contracting 3D object like a cardiac cell. This problem has been handled by considering an optimal size of the ROI in association with an optimum value of the similarity function $C_v(I_{W1},I_{W2})$, according to the following procedure: taking a square window *Wind*1 of size $(si \times si)$ and centered at (X_t^{kl}) in *Image* 1, we defined a ROI centered at $(X_{t+\Delta t}^{kl}, Y_{t+\Delta t}^{kl})$ in *Image 2* with size $(si + (ka \times si) \times (si + (ka \times si)))$, where *ka* is a dilation scale-factor $(ka \geq 1)$. We started the search of the optimum displacement vector $\boldsymbol{w}^\star$ by considering a ROI two times larger than *Wind1* $(ka = 1)$. This gives a first value δ_1 of $\boldsymbol{C}_v(I_{W1},I_{W2})$. Then, the value of the scaling factor *ka* is increased by an integer value of 1, which generates increasing values δ_{ka} that tend to plateau toward the best reachable correlation value δ_{opt} of $\boldsymbol{C}_v(I_{W1},I_{W2})$, with $\delta_{\text{opt}} \leq 1$. The larger is the value of δ_{opt}, the more accurate is the detection of the matching window *Wind*2*. This point is illustrated in Figure 3 introduced below. A global estimation of a correlation threshold δ was obtained by averaging all the values δ_{opt} over *Image* 1.

Construction of Pairs of Test Images

To test the accuracy and precision of the method, different pairs of test images were constructed by applying specific and known spatial displacement fields on a textured square object with size $[0,1] \times [0,1]$ [*Image* 1, Fig. 2(A)] to get corresponding deformed objects [*Image* 2, Figs. 2(B) and 2(C)]. The size of *Image* 1 is 256×256 pixels. Meshing the square with 2D triangular elements defines a set of nodes where known displacements have been applied.

Case 1: On each node, a linear spatial distribution of the displacement field was applied in the *Ox* direction as $u(x,y) = 0.1\,x$, while the left boundary of the deforming square remains fixed (i.e. $u(0,y) = v(0,y) = 0$). Both upper and lower sides of the square were free to move (zero-stress boundary conditions). The associated component $v(x,y)$ of the displacement vector was computed using a finite element analysis software (Comsol Multiphysics©), assuming that the square behaves as a 2D linear elastic membrane with Poisson's ratio 0.49 and Young modulus 500 kPa.

Case 2: The second set of test images was obtained by imposing to the textured squared object a more complex displacement field, defined by $u(x,y) = 0.1\,y$ and $v(x,y) = 0.1\,x$ [Fig. 2(C)].

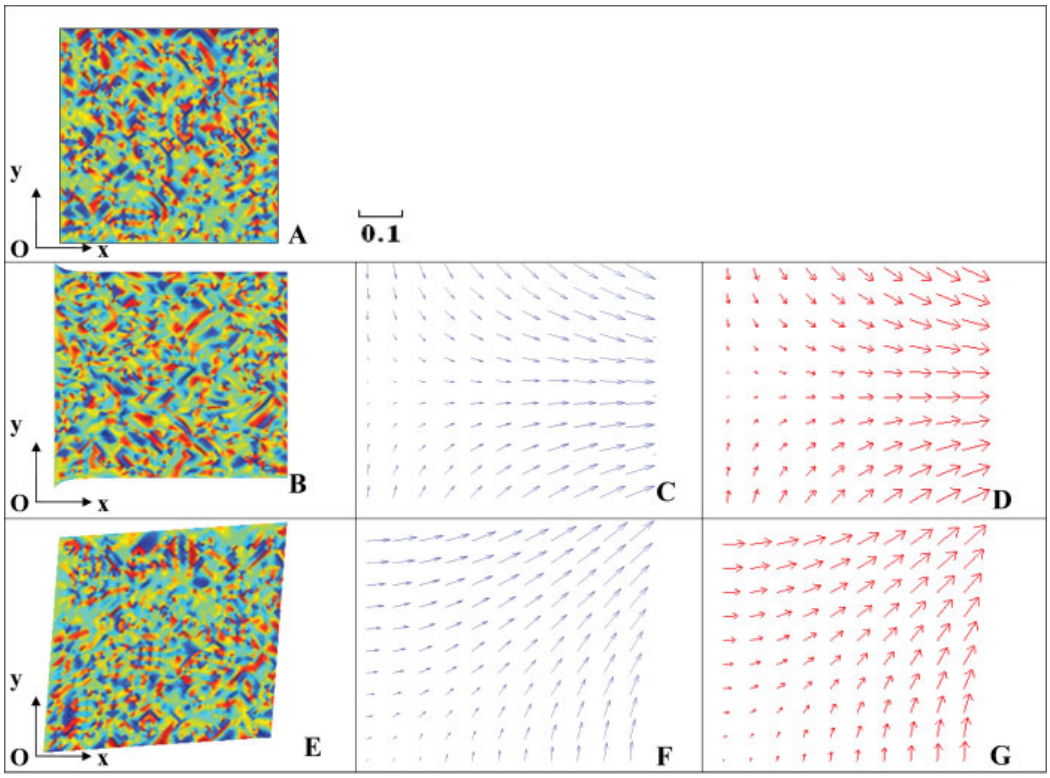

Figure 2. Analysis performed on pairs of test images, constructed from an initial 2D image exhibiting heterogeneous (textured) illumination map. **A**: Initial image *Image 1*. **B**: *Image 2* resulting from the transformation of *Image 1* by application of a displacement field defined by $u(x,y)=0.1x$. **C**: Associated displacement field computed by ICM. **D**: Corresponding theoretical displacement field. **E**: Second pair of test images we considered. Here, *Image 2* has been synthesized after imposing the displacements $u(x,y) = 0.1y$ and $v(x,y) = 0.1x$ to *Image 1*. **F**: Associated displacement field computed by ICM. **G**: Corresponding theoretical displacement field. In Figures 2(C)–2(F), the optimization procedure of the ICM has been conducted with a research window *Wind1* of 10 × 10 pixels, a correlation threshold $\delta = 0.95$, a dilation-scale factor $ka = 3$ and ROI size of 40 × 40 pixels. [Color figure can be viewed in the online issue which is available at www.interscience.wiley.com.]

Derivation of the Strain Field Associated with the ICM Computed Displacement Field

For each matching window *Wind2**, centered at $(X^{kl}_{t+\Delta t}, Y^{kl}_{t+\Delta t})$ and associated with a reference window *Wind*1 centered at (X^{kl}_t, Y^{kl}_t) at time t, we derived the displacement field $\boldsymbol{w}^{kl}_{t,t+\Delta t}$ between times t and $t+\Delta t$ as:

$$\boldsymbol{w}^{kl}_{t,t+\Delta t} = \begin{pmatrix} u^{kl}_{t,t+\Delta t} \\ v^{kl}_{t,t+\Delta t} \end{pmatrix} = \begin{pmatrix} X^{kl}_{t+\Delta t} - X^{kl}_t \\ Y^{kl}_{t+\Delta t} - Y^{kl}_t \end{pmatrix} \tag{6}$$

To describe the transformation of any window, located at (k,l), between times t and $t+\Delta t$, we used the deformation gradient tensor $\mathbf{F}^{kl}_{t,t+\Delta t}$ given by

$$\mathbf{F}^{kl}_{t,t+\Delta t} = \begin{pmatrix} \dfrac{\partial u_{t,t+\Delta t}}{\partial x} & \dfrac{\partial u_{t,t+\Delta t}}{\partial y} \\ \dfrac{\partial v_{t,t+\Delta t}}{\partial x} & \dfrac{\partial v_{t,t+\Delta t}}{\partial y} \end{pmatrix} \tag{7}$$

The relation between the Green-Lagrange strain tensor $\mathbf{E}^{kl}_{t,t+\Delta t}$ and the deformation gradient tensor is given from continuum mechanics by (23):

$$\mathbf{E}^{kl}_{t,t+\Delta t} = \frac{1}{2}\left(\left(\mathbf{F}^{kl}_{t,t+\Delta t}\right)^{\mathbf{T}} \mathbf{F}^{kl}_{t,t+\Delta t} - \boldsymbol{Id}\right) \tag{8}$$

where $\boldsymbol{Id}$ is the identity tensor and $(.)^{\mathbf{T}}$ denotes the tensor transposition.

The strain field with regard to the initial (or undeformed) configuration at t_0, i.e. for generally large deformations, is given at any time t by the Green-Lagrange strain tensor strain $\mathbf{E}^{kl}_{t_0,\ t}$ computed from the composition of the successive deformation gradient tensors:

$$\mathbf{F}^{kl}_{t_0,t} = \mathbf{F}^{kl}_{t_0,t_0+\Delta t} \bullet \mathbf{F}^{kl}_{t_0+\Delta t,t_0+2\Delta t} \bullet \ldots \bullet \mathbf{F}^{kl}_{t-2\Delta t,t-\Delta t} \bullet \mathbf{F}^{kl}_{t-\Delta t,t} \tag{9}$$

with

$$\mathbf{E}^{kl}_{t_0,t} = \frac{1}{2}\left(\left(\mathbf{F}^{kl}_{t_0,t}\right)^{T} \mathbf{F}^{kl}_{t_0,t} - \mathbf{I}d\right) \tag{10}$$

from which we obtained the normal strains components $E_{xx,t}$, $E_{yy,t}$ and shear strain component $E_{xy,t}$, where the subscript t_0 has been omitted to simplify notations.

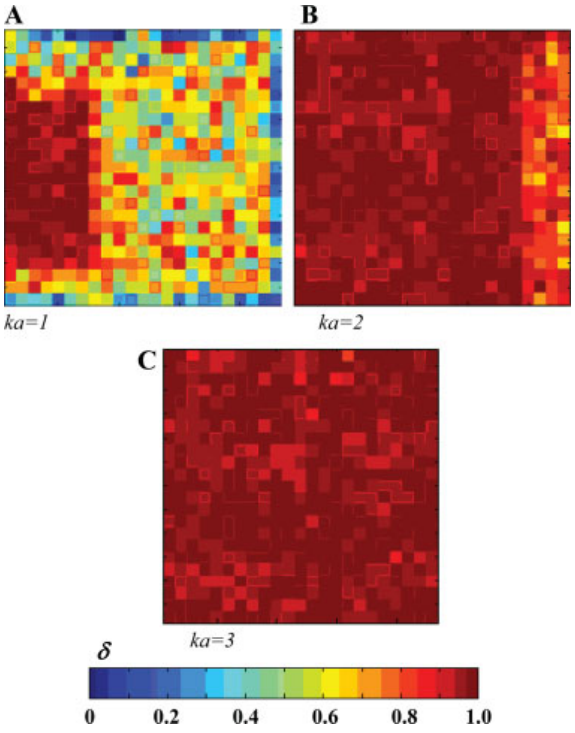

Figure 3. Search for an optimum size of both research window *Wind1* and ROI illustrated with the first pair of test images we considered in the previous figure [Figs. 2(A) and 2(B)]. Best correlations are obtained when the correlation threshold δ reaches the value $\delta \sim 1$. With a scale factor $ka = 1$ [Fig. 3(A)] a good correlation is only obtained on the left side of the deforming surface, i.e. in small displacement regions. Correlation significantly improves with $ka = 2$ [Fig. 3(B)] but with still weak correlation remaining in regions experiencing large displacements. Optimum in correlation optimum is obtained with $ka = 3$ [Fig. 3(C)], i.e. with a ROI size of 40 × 40 pixels. [Color figure can be viewed in the online issue which is available at www.interscience.wiley.com]

When deformations are computed between two consecutive images, small deformations analysis was performed. We then evaluated the associated linearized normal $\varepsilon_{xx,t}$, $\varepsilon_{yy,t}$, and shear strains $\varepsilon_{xy,t}$ between two successive images as

$$\varepsilon_{xx,t} = \frac{\partial u_{t,t+\Delta t}}{\partial x}; \quad \varepsilon_{yy,t} = \frac{\partial v_{t,t+\Delta t}}{\partial y};$$
$$\varepsilon_{xy,t} = \frac{1}{2}\left(\frac{\partial u_{t,t+\Delta t}}{\partial y} + \frac{\partial v_{t,t+\Delta t}}{\partial x}\right) \tag{11}$$

These derivatives were computed numerically using the following finite differences approximations

$$\varepsilon^{kl}_{xx,t} = \frac{u^{(k+1)l}_{t,t+\Delta t} - u^{(k-1)l}_{t,t+\Delta t}}{X^{(k+1)l} - X^{(k-1)l}}; \quad \varepsilon^{kl}_{yy,t} = \frac{v^{k(l+1)}_{t,t+\Delta t} - v^{k(l-1)}_{t,t+\Delta t}}{Y^{k(l+1)} - Y^{k(l-1)}};$$
$$\varepsilon^{kl}_{xy,t} = \frac{1}{2}\left(\frac{u^{k(l+1)}_{t,t+\Delta t} - u^{k(l-1)}_{t,t+\Delta t}}{Y^{k(l+1)} - Y^{k(l-1)}} + \frac{v^{(k+1)l}_{t,t+\Delta t} - v^{(k-1)l}_{t,t+\Delta t}}{X^{(k+1)l} - X^{(k-1)l}}\right) \tag{12}$$

Results

Accuracy, Robustness, and Optimal Window Size of the Optical Flow Algorithm

Both pairs of test images were analyzed using our optical flow algorithm. Accuracy and robustness were assessed from comparison of the computed displacement vector fields with the corresponding known numerical or analytical solutions [case 1, Fig. 2(B); case 2, Fig. 2(E)]. Figures 2(D) and 2(G) present the known displacement field imposed for synthesis of each *Image*2 of the test images pairs. In both cases, the present algorithm successfully reconstructed the corresponding displacement maps [Figs. 2(C)–2(F)], with a maximum error of 15% on the computed displacements.

These test images have been also used to determine the optimal size of the research window. When considering the first pair of test images [Figs. 2(A) and 2(B)], our computations showed (Fig. 3) that the optimum size for square window *Wind*1 is close to (10 × 10) pixels, while the best correlation threshold δ has been obtained with a dilation scale-factor $ka = 3$, corresponding to a ROI in *Image* 2 with size of (40 × 40) pixels.

Quantification of Cardiomyocyte Shortening from Computed Contraction Waves

This section presents the analysis of two typical spontaneous contractions of isolated adult rat cardiomyocytes. It is known that cell contractions triggered by calcium sparks can appear spontaneously, i.e. in the absence of external stimulation, and randomly within the cell when cardiomyocytes are cultured *in vitro* (24).

We will focus here on two different contraction patterns that we observed in our *in vitro* experiments. In the first contraction sequence (seq1), the contraction wave started from the left side of the cell and propagated up to the right boundary [Figs. 4(1A)–4(1E)]. Interestingly, the same cardiomyocyte later exhibited a rather different contraction pattern (seq2), the contraction being then initiated at the center of the cell (Figs. 5(2A)–5(2E)]. In this contraction pattern, two strain waves now propagated in opposite directions, toward the cardiomyocyte extremities. A measured time lag of 18.34 s separated the two cell contractions.

Global Quantification of Single Cardiomyocyte Shortening

Figure 6A shows the dynamics of the cardiomyocyte shortening recorded by sequences seq1 and seq2, respectively. The cell shortening was measured in three different ways. First, a global evaluation of the cell length was performed, for both seq1 and seq2, by finding the length of the smallest rectangle surrounding the cardiomyocyte (Fig. 6(A), solid lines). Alternatively, cardiomyocyte shortening in seq1 was computed from the integration, along a longitudinal middle-cell cross-section, of the local intracellular strains derived from the ICM approach (Fig. 6(A) left, square markers). Such one-dimensional integration from local to global cell length is not valid for seq2, since then the cardiomyocyte underwent significant

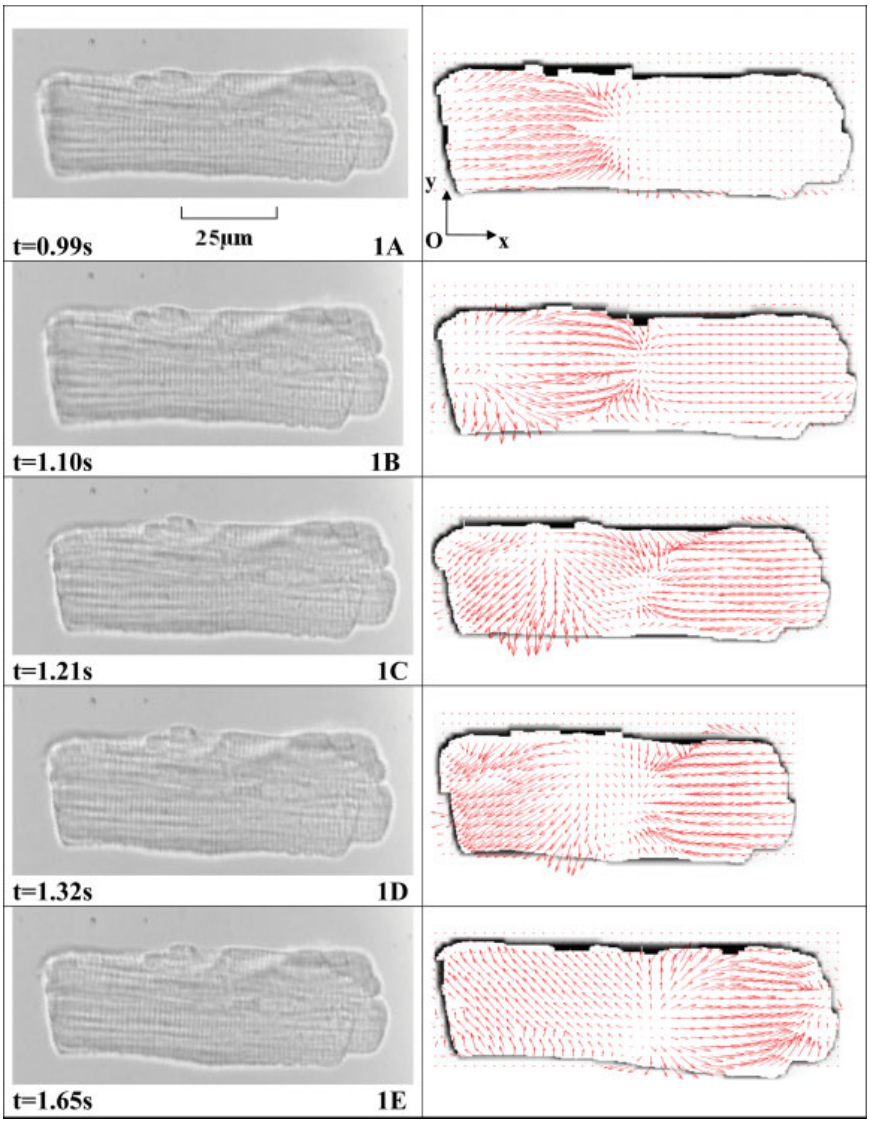

Figure 4. Evolution with time of the displacement field $\boldsymbol{w}(u,v)$ computed for the first cardiomyocyte contraction sequence, defined as seq1 in the main text. In seq1, the cell contraction starts from the left side [Fig. 4(1**A**)], generating in both cell extremities displacements that develop in opposite directions (1**B**–1**D**). After a maximum shortening, cell relaxation takes place on the left side (1**E**). Parameters of the ICM computation are as follow: *Wind1* size is 9 × 9 pixels, ka=2, ROI size of 27 × 27 pixels and δ = 0.85. [Color figure can be viewed in the online issue which is available at www. interscience.wiley.com.]

bending during contraction. In this case, the quantification of the cell shortening from the ICM approach was restricted to the consideration of windows *Wind*1 located at both cell borders (Fig. 6(A) right, circular markers).

During the first contraction (seq1), the cell contraction/relaxation took place within 2.05 s and represents 6% (7.13 μm) of the maximum cell length (112.05 μm). The contraction/relaxation phase was shorter (1.21 s) and two times larger (13.69 μm) in seq2, since then the two cell sides contracted simultaneously.

The times needed to reach the maximum amplitude of contraction were 0.57 s and 0.33 s in seq1 and seq2 respectively. In seq1, contraction/relaxation began on the left side. During the left side relaxation contraction/relaxation occurs in right cell borders. In addition, we checked that the image analysis results given by moving windows located at the adult cardiomyocyte extremities gave realistic and accurate antagonistic displacement profiles for both cardiomyocyte extremities [Figs. 6(B) and 6(C)]. These windows exhibited the same profiles as those reported in previous studies using attached carbon fibers (25,26).

The agreement between globally based and locally based measurements methods is quite satisfactory, and thus illustrates that an accurate and combined analysis of the cell contraction and associated intracellular displacement fields is provided by the ICM-based analysis, as detailed below.

Characterization of the Associated Intracellular Contraction Patterns

The strain waves, which propagate through the contracting cardiomyocyte, have been tracked for the two contractile behaviors recorded in the time-lapse sequences seq1 and seq2.

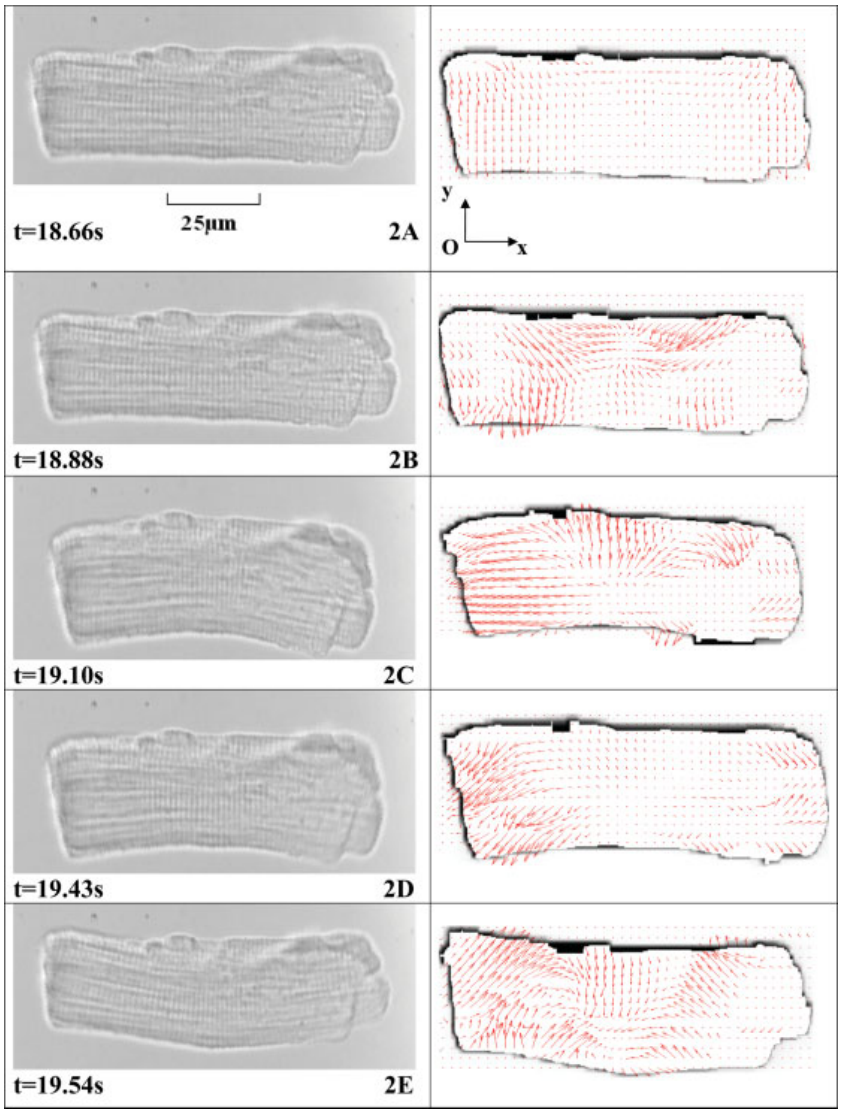

Figure 5. Evolution with time of the displacement field $\boldsymbol{w}(u,v)$ computed for the second cardiomyocyte contraction sequence, defined as seq2 in the main text. In seq2, a twitch appears at the cell centre (2**B**). It propagates towards both cell extremities, while inducing an intracellular torque that generates a transient upward, then downward bending of both cell sides (2**C**–2**D**). In this case, sarcomeres exhibit significant curvature during the maximum cell shortening, but then recover their resting length during the relaxation phase (2**E**). Parameters of the ICM computation are as follow: *Wind1* size is 9 × 9 pixels, $ka = 2$, ROI size of 27 × 27 pixels and $\delta = 0.85$. [Color figure can be viewed in the online issue which is available at www.interscience.wiley.com.]

Thanks to our optical flow analysis, the local displacement field can be computed in any part of the cardiomyocyte, thus giving access to intracellular mechanical features of intracellular contraction/relaxation at the sarcomere level. In this analysis, the size of *Wind*1 is 10 × 10 pixels, while a ROI-scale factor $ka = 2$ and a ROI of 30 × 30 pixels were chosen.

In the first videomicroscopy sequence, the computed motion field revealed four main steps during cell contraction. The first one was characterized by the cell contraction starting on the left cell side, the right cell side remaining at rest during 440 ms [Fig. 4(1A)]. In the second stage (220 ms), sarcomeres contractions occurred on both sides of the propagating front [Fig. 4(1C)]. In the third stage, sarcomere relaxation began on the left cell side, while contraction still proceeded on the right side, during 330 ms [Fig. 4(1D)]. Finally, complete relaxation took place on the right cell side (550 ms) [Fig. 4(1E)].

Analysis of the second time-lapse sequence (seq2) highlights two main phases during cardiomyocyte contraction/relaxation. During the first phase, an asymmetric distribution of intracellular stresses at the cell center lifted the cell extremities upwards (550 ms) [Figs. 5(2A) and 5(2B)]. However, this twisted motion was immediately followed by a reverse torque, which tended to shift the cell back, probably as a result of homogenization of calcium concentrations within the cell (550 ms) [Figs. 5(2C) and 5(2D)].

Analysis of Intracellular Strains

A main benefit of our approach is its ability to provide a quantification of the intracellular strains everywhere within the cardiac cell. This section presents the estimated strain fields we derived from the displacement fields computed by the optical flow method, using Eq. (10).

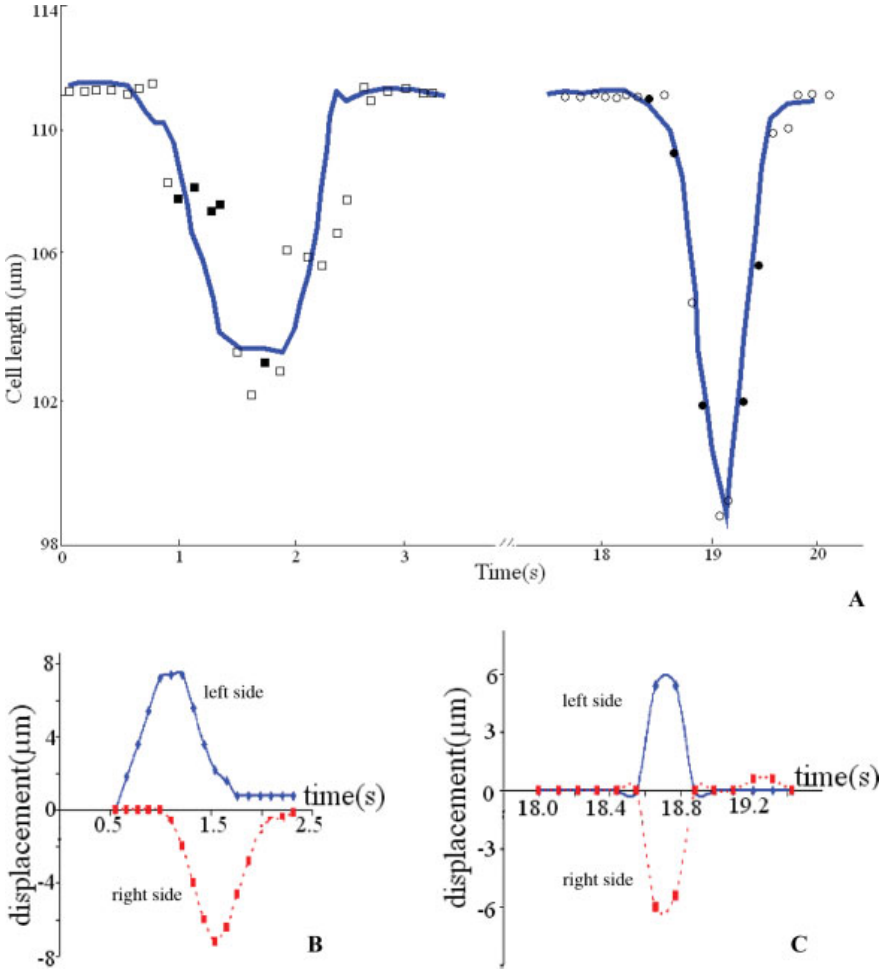

Figure 6. Dynamics of the cardiomyocyte shortening during contraction wave propagation, corresponding to seq1 and seq2 analyzed in Figures 4 and 5. The figure compares cell shortening measurements performed both globally and with ICM, as explained in the text. Globally, the time-varying cardiomyocyte length has been evaluated as the length of the smallest rectangular envelope that surrounds the cardiomyocyte (solid lines) in both seq 1 [Fig. 6(**A**), left part) and seq 2 [Fig. 6(A), right part]. Thanks to the ICM approach, cell contraction amplitude has also be computed – in seq1, from the integration of the intracellular strain $E_{xx,t}$ along a cell cross-section taken in the middle of the cell (square markers) – in seq2, from image correlation analysis restricted to both cell extremities (circular markers). The relative and corresponding displacement of each extremity of the cardiomyocyte has been detailed in Figures 6(**B**) and 6(**C**). Filled squares and circles correspond to the observation times presented in Figures 4 and 5 for both contraction sequences. In seq1, the propagation of the contraction wave from left to right induces a phase shift in cell extremities displacements [Fig. 6(B)]. Conversely, both extremities move almost in phase in seq 2 when cardiomyocyte contraction is initiated from the cell centre [Fig. 6(C)]. [Color figure can be viewed in the online issue which is available at www.interscience.wiley.com.]

For two observed typical contractile behaviors of isolated cardiomyocytes, we reported in Figure 7 the components of the 2D strain tensor, namely (i) horizontal strain $E_{xx,t}$ along the cell length, i.e. in the sarcomere direction and (ii) transverse strain $E_{yy,t}$ along the cell width. Local cell stretching is characterized by a positive strain, while a negative strain indicates a cell twitch.

When contraction propagated from left to right (seq1), the wave front was preceded by negative values of strains $E_{xx,t}$, $E_{yy,t}$ [Figs. 7(1A)–7(1C)] and followed by positive strain values. Absolute strains values were in the range $E_{xx,t}$ = 12–15%, with $E_{yy,t}$ = 8%.

In the second videomicroscopy sequence seq2, the contraction wave, which emerges in the middle of the cardiomyocyte, was associated with negative strains along both propagating directions. This contraction traveled along the cell horizontally and vertically [Figs. 7(2A)–7(2C)]. Immediately after this contraction wave, a dilation wave front started from the cell center and was characterized by positive strains. Corresponding strains values were $E_{xx,t}$ = 15–20% and $E_{yy,t}$ =7–10% for both contraction waves.

Let us notice that the shear strain value $E_{xy,t}$ was not negligible, with $E_{xy,t}$ ~10% for both sequences. In seq1, the wave propagation occurred mainly along the sarcomere direction

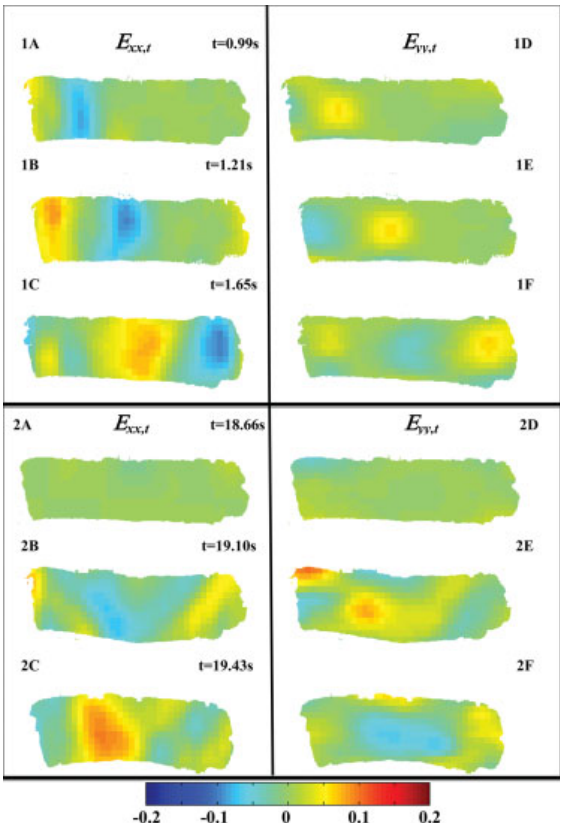

Figure 7. Amplitude of the strain field components computed by ICM for the two contraction sequences seq1 [Figs. 7(1**A**)–7(1**F**)] and seq2 [Figs. 7(2**A**)–(2**F**)]. With seq1, the strain field $E_{xx,t}$ computed along the *x*-direction [Figs. 7(1A)–(1**C**)] highlights the uniaxial feature of the wave propagation, characterized by negative strains followed by positive strains. Variations of the normal strain component $E_{yy,t}$ in the *y*-direction [Figs. 7(1**D**)–(1F)] reflect the cardiomyocyte incompressibility. The spatio-temporal strain distribution in seq2 appears more complicated both along *x* direction [Figs. 7(2A)–(2C)] and *y*-direction [Figs. 7(2D)–(2F)], the contraction wave propagating from the cell centre in an oblique manner. Parameters for the ICM computations are: *Wind1* 9 × 9 pixels, *ka* = 2, ROI size of 27 × 27 pixels and δ = 0.85. [Color figure can be viewed in the online issue which is available at www.interscience.wiley.com]

and a significant shear strain developed mostly in the cell corner during cell contraction. In seq2, shear strains were more homogeneously distributed and appeared all along the cell (data not shown).

Evaluation of the Algorithm Performances When Analyzing Time-Lapse Sequences Including Less Textured Images of the Cardiac Cell Contraction

Neonatal cardiomyocytes present a less organized intracellular architecture than adult cardiac myocytes, and thus provide an interesting application field to evaluate our approach in the case of less textured images. Thus, we analyzed time-lapse sequences of contracting rat neonatal cardiomyocytes, isolated from the ventricles by enzymatic dissociation (27), and computed the strain fields generated during cell contraction. The cell contraction occurred with higher frequency, the contraction motion being then mainly centripetal (Fig. 8). The strains values have been still computed accurately by the optical flow method, with absolute values in the range of 1–3% for $\varepsilon_{xx,t}$ and $\varepsilon_{yy,t}$, with shear strains $\varepsilon_{xy,t}$ in the order of ~2%. This indicates that adult rat cardiomyocytes generate intracellular strains two to three times larger than neonatal cells. These results compares quite well with the 3-fold increase in force normalized to the cross-sectional area (F_{CSA}) reported for murine skinned cardiomyocytes (28) and skinned trabeculae from rat ventricles (29).

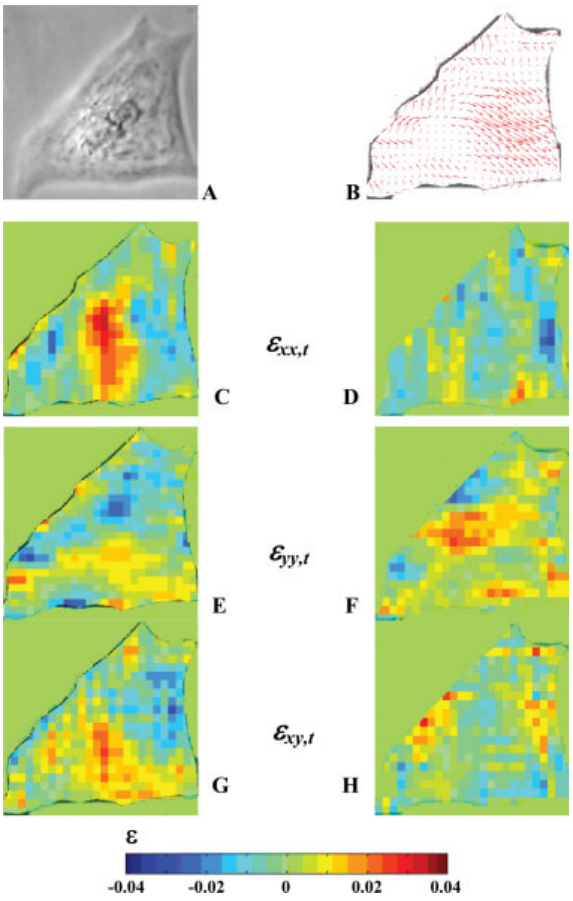

Figure 8. Quantification by ICM of the linearized strain components developed by contracting rat neonatal cardiomyocytes imaged by phase contrast videomicroscopy. At this stage of development, the cardiac cells lack the well-organized band-like arrangement observable in adult cells (Fig. 1), leading to less textured 2D images [Fig. 8(**A**)]. However, our ICM approach still successfully quantifies the rather complicated cell contraction/relaxation kinematics [Fig. 8(**B**)]. Cell contraction appears rather centripetal [Fig. 8(**E**)], with significant normal strains $\varepsilon_{xx,t}$ [Figs. 8(**C**) and 8(**D**)] and $\varepsilon_{yy,t}$ [Figs. 8(**E**) and 8(**F**)], but also with zones of shear strains $\varepsilon_{xy,t}$ [Figs. 8(**G**) and 8(**H**)] that indicates localized cell cytoskeleton torsion. Parameters for the ICM computations are: *Wind1* 9 × 9 pixels, *ka* = 1, ROI size of 18 × 18 pixels and δ = 0.75. [Color figure can be viewed in the online issue which is available at www.interscience.wiley.com]

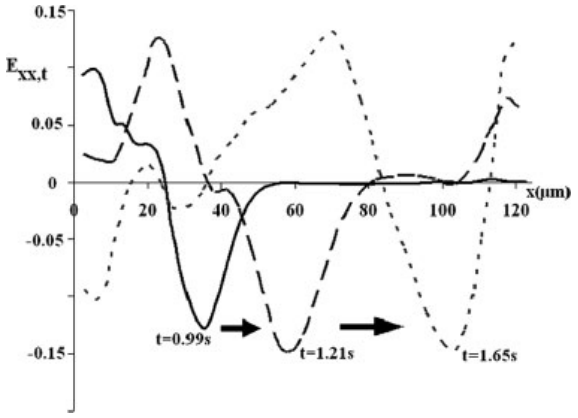

Figure 9. Scan-line of the propagation pattern in seq1 of the axial large strain component $E_{xx,t}$ of the intracellular strain field computed by ICM along a cardiomyocyte section crossing the middle of the cell from one extremity to the other. The successive profiles shown at time $t = 0.99$ s $t = 1.21$ s and $t = 1.65$ s can be viewed as mirror images of the underlying profile of intracellular concentrations which would have been obtained if tracking calcium wave propagation with the aid of fluorescent probes. Parameters for the ICM computations are as in Figure 7.

Discussion

In this study, a correlation-based optical flow method has been developed to analyze time-lapse sequences of contracting cardiomyocytes and to quantify originally spatio-temporal variations of intracellular strains generated at a sarcomere scale. The proposed image processing method allowed a precise tracking of the strain wave traveling along the cardiac cell by analyzing the correlation of grey level patterns between consecutive pairs of images.

While belonging to a class of image processing methods rather widely used for analyzing objects motions from image sequences (16), few applications have been reported in the context of cell dynamics to date (12–14). Indeed, the association of the usually limited contrast of videomicroscopy images with large cell deformations defines a challenging framework for implementation of optical flow methods. Thus, in order to obtain a 2D vector representation of image pixels displacements, regularization conditions are usually added to constrain the search for the optimum displacement field solution. The method developed here presents substantial improvements compared with the method used in other studies (13,30), since it avoids the need for choosing regularization constraints. In fact, our method takes benefit of the landmarks provided by the sarcomeres structural organization, and thus provides a precise characterization of cardiomyocyte contraction and deformation without requiring the coupling of phase contrast observation with intracellular calcium imaging by fluorescent probes. In addition, there is no need for linking specific markers, such as microbeads, on the cell surface to track complex cell distortions (31–33).

Our approach also differs from other optical flow approaches developed for analyzing oscillatory dynamics of cell protrusions (12) or tissue contractions (34), which model the flow by a linear transformation. As a result, one gets a compact and global measurement of the biological object deformation from the time evolution of motion descriptors associated with the different types of singular points, characterizing the velocity field computed between two consecutive images (19).

In the present study, we were looking for a simple and efficient way to link observations made at the whole-cell level to dynamical features exhibited at the sarcomere level. The proposed approach appears rather powerful and satisfactory since the integration of the displacement fields computed at this sub-cellular scale are in excellent agreement with the global measurements of cardiomyocyte shortening obtained by tracking the motion of both cell extremities. As a consequence, we were able to accurately identify the amplitude and spatio-temporal variations of the strains wave that characterize successive sarcomere contraction/relaxation.

The accuracy of the method already insures that displacements of a few microns can be reliably detected. However, our algorithm can still be extended to allow sub-pixel accuracy. The temporal resolution of the method obviously depends on the sampling rate of image acquisition, and can take benefit of the ultra-fast cameras already used to image intracellular calcium dynamics.

Finally, we would like to discuss possible implications of our image analysis approach. First, we can notice that the propagation of the negative longitudinal strains $E_{xx,t}$ (Fig. 9), corresponding to a localized intracellular compression, can be viewed as a mirror image of the underlying propagating peak of cytosolic calcium that drives the cell-contracting twitch (35).

Second, we might wonder if such similarity-based optical flow approach still remains reliable when analyzing mechanical deformation of cells, which do not exhibit regular and organized grey-level intensity patterns when observed by phase contrast or DIC microscopy. As a reply, we considered the contraction of cardiomyocytes taken at an earlier developmental stage. Although rat neonatal cardiomyocytes lack the well-organized band-like arrangement observable in adult cells, our ICM approach still successfully quantified the rather complicated cell dynamics, including phases of centripetal contraction and generation of localized intracellular shear strain.

In conclusion, the proposed approach offers significant improvements to the classical ways of quantifying single cardiomyocyte deformations dynamics and using either force transducers, lasers diffraction techniques or fluorescent probes. By providing a direct and noninvasive access to intracellular strain at the sarcomere scale, this image processing method provides information on both active and passive mechanical properties of cardiac cell in a noninvasive way, i.e. without requiring the use of external probes, as it is the case in micromanipulation experiments like MTC experiments (36). More fundamentally, this optical flow method might also help to investigate the influence of mechanosensitive biochemical processes, depending on sarcomere stretching or interfilament

spacing (37), which control the contractility and efficiency of cardiomyocyte contraction (38).

Acknowledgments

The authors thank Drs. R.S. Chadwik (NINDS-National Institutes of Health) and Dr. C. Hongxue (Northwestern University) for their useful comments, as well as Drs. N. Béreaud, J. Olivares (LBFA, Univ. J. Fourier), and M. Trifa (CNRS, TIMC) for their technical support.

Literature Cited

1. Belevych A, Kubalova Z, Terentyev D, Hamlin RL, Carnes CA, Gyorke S. Enhanced ryanodine receptor-mediated calcium leak determines reduced sarcoplasmic reticulum calcium content in chronic canine heart failure. Biophys J 2007;93:4083–4092.
2. Cagalinec M, Chorvat D Jr, Mateasik A, Bacharova L. Sustained spiral calcium wave patterns in rat ventricular myocytes. J Cell Mol Med 2007;11:598–599.
3. Dupont G, Combettes L, Leybaert L. Calcium dynamics: Spatio-temporal organization from the subcellular to the organ level. Int Rev Cytol 2007;261:193–245.
4. Miura M, Ishide N, Oda H, Sakurai M, Shinozaki T, Takishima T. Spatial features of calcium transients during early and delayed afterdepolarizations. Am J Physiol 1993;265(2 Part 2):H439–H444.
5. Priebe L, Beuckelmann DJ. Simulation study of cellular electric properties in heart failure. Circ Res 1998;82:1206–1223.
6. Wakayama Y, Miura M, Stuyvers BD, Boyden PA, ter Keurs HE. Spatial nonuniformity of excitation-contraction coupling causes arrhythmogenic Ca^{2+} waves in rat cardiac muscle. Circ Res 2005;96:1266–1273.
7. Loughrey CM, MacEachern KE, Cooper J, Smith GL. Measurement of the dissociation constant of Fluo-3 for Ca^{2+} in isolated rabbit cardiomyocytes using Ca^{2+} wave characteristics. Cell Calcium 2003;34:1–9.
8. Rockwell PL, Storey BT. Determination of the intracellular dissociation constant. K(D), of the fluo-3. Ca(2+) complex in mouse sperm for use in estimating intracellular Ca(2+) concentrations. Mol Reprod Dev 1999;54:418–428.
9. Zhao Y, Lim CC, Sawyer DB, Liao R, Zhang X. Simultaneous orientation and cellular force measurements in adult cardiac myocytes using three-dimensional polymeric microstructures. Cell Motil Cytoskeleton 2007;64:718–725.
10. Yin S, Zhang X, Zhan C, Wu J, Xu J, Cheung J. Measuring single cardiac myocyte contractile force via moving a magnetic bead. Biophys J 2005;88:1489–1495.
11. Slawnych MP, Morishita L, Bressler BH. Image-analysis-based assessment of the effects of the "Ca^{2+}-jump" technique on sarcomere uniformity. J Appl Physiol 1998;85:955–961.
12. Germain F, Doisy A, Ronot X, Tracqui P. Characterization of cell deformation and migration using a parametric estimation of image motion. IEEE Trans Biomed Eng 1999;46:584–600.
13. Cai H, Richter CP, Chadwick RS. Motion analysis in the hemicochlea. Biophys J 2003;85:1929–1937.
14. Collin O, Tracqui P, Stephanou A, Usson Y, Clement-Lacroix J, Planus E Spatiotemporal dynamics of actin-rich adhesion microdomains: Influence of substrate flexibility. J Cell Sci 2006;119 (Part 9):1914–1925.
15. Martel AL, Froh MS, Brock KK, Plewes DB, Barber DC. Evaluating an optical-flow-based registration algorithm for contrast-enhanced magnetic resonance imaging of the breast. Phys Med Biol 2007;52:3803–3816.
16. Barron JL, Fleet D, Beauchemin S. Performance of optical flow techniques. Int J Comput Vis 1994;12:43–77.
17. Bergonnier S, Hild F, Rieunier J, Roux S. Strain heterogeneities and local anisotropy in crimped glass wool. J Mater Sci 2005;40:5949–5954.
18. Besnard G, Hild F, Roux S. "Finite-Element". Displacement fields analysis from digital images: Application to Portevin-Le Châtelier Bands. Exp Mech 2006;46:789–803.
19. Boerboom RA, Rubbens MP, Driessen NJ, Bouten CV, Baaijens FP. Effect of strain magnitude on the tissue properties of engineered cardiovascular constructs. Ann Biomed Eng 2008;36:244–253.
20. Olivares J, Dubus I, Barrieux A, Samuel JL, Rappaport L, Rossi A. Pyrimidine nucleotide synthesis is preferentially supplied by exogenous cytidine in adult rat cultured cardiomyocytes. J Mol Cell Cardiol 1992;24:1349–1359.
21. McKenna S, McGillis W. Performance of digital image velocimetry processing techniques. Exp Fluids 2002;32:106–115.
22. Ma S, Jin G. New correlation coefficients designed for digital speckle correlation method (DSCM). SPIE 2003;5058:25–33.
23. Holzapfel GA. Nonlinear Solid Mechanics. NY: Wiley; 2001.
24. Stuyvers BD, Dun W, Matkovich S, Sorrentino V, Boyden PA, ter Keurs HE. Ca2+ sparks and waves in canine purkinje cells: A triple layered system of Ca^{2+} activation. Circ Res 2005;97:35–43.
25. Nishimura S, Yasuda S, Katoh M, Yamada KP, Yamashita H, Saeki Y, Sunagawa K, Nagai R, Hisada T, Sugiura S. Single cell mechanics of rat cardiomyocytes under isometric, unloaded, and physiologically loaded conditions. Am J Physiol Heart Circ Physiol 2004;287:H196–H202.
26. Sugiura S, Nishimura S, Yasuda S, Hosoya Y, Katoh K. Carbon fiber technique for the investigation of single-cell mechanics in intact cardiac myocytes. Nat Protocol 2006;1:1453–1457.
27. Riou L, Ghezzi C, Mouton O, Mathieu JP, Pasqualini R, Comet M, Fagret D. Cellular uptake mechanisms of 99mTcN-NOET in cardiomyocytes from newborn rats: Calcium channel interaction. Circulation 1998;98:2591–2597.
28. Siedner S, Kruger M, Schroeter M, Metzler D, Roell W, Fleischmann BK, Hescheler J, Pfitzer G, Stehle R. Developmental changes in contractility and sarcomeric proteins from the early embryonic to the adult stage in the mouse heart. J Physiol 2003;548 (Part 2):493–505.
29. Niederer SA, Hunter PJ, Smith NP. A quantitative analysis of cardiac myocyte relaxation: a simulation study. Biophys J 2006;90:1697–1722.
30. Hu X, Evans BN, Dallos P. Direct visualization of organ of corti kinematics in a hemicochlea. J Neurophysiol 1999;82:2798–2807.
31. Dembo M, Wang YL. Stresses at the cell-to-substrate interface during locomotion of fibroblasts. Biophys J 1999;76:2307–2316.
32. Riveline D, Zamir E, Balaban NQ, Schwarz US, Ishizaki T, Narumiya S, Kam Z, Geiger B, Bershadsky AD. Focal contacts as mechanosensors: externally applied local mechanical force induces growth of focal contacts by an mDia1-dependent and ROCK-independent mechanism. J Cell Biol 2001;153:1175–1186.
33. Balaban NQ, Schwarz US, Riveline D, Goichberg P, Tzur G, Sabanay I, Mahalu D, Safran S, Bershadsky A, Addadi L, Geiger B. Force and focal adhesion assembly: A close relationship studied using elastic micropatterned substrates. Nat Cell Biol 2001; 3:466–472.
34. Zoccolan D, Giachetti A, Torre V The use of optical flow to characterize muscle contraction. J Neurosci Methods 2001;110:65–80.
35. Pustoc'h A, Ohayon J, Usson Y, Kamgoue A, Tracqui P. An integrative model of the self-sustained oscillating contractions of cardiac myocytes. Acta Biotheor 2005;53: 277–293.
36. Lammerding J, Kazarov AR, Huang H, Lee RT, Hemler ME. Tetraspanin CD151 regulates $\alpha 6\beta 1$ integrin adhesion strengthening. Proc Natl Acad Sci USA 2003;100:7616–7621.
37. Hoshijima M, Knoll R, Pashmforoush M, Chien KR Reversal of calcium cycling defects in advanced heart failure toward molecular therapy. J Am Coll Cardiol 2006;48(9Suppl 1):A15–A23.
38. Tracqui P, Ohayon J, Boudou T. Theoretical analysis of the adaptive contractile behaviour of a single cardiomyocyte cultured on elastic substrates with varying stiffness. J. Theor Biol 2008;255:92–105.